High thermoelectric performance carbon nanotube/polycaprolactone composites for sustainable energy harvesting

Siqi Liu,[a] Hui Li,[b] Hao Wang, [a] Junhua Kong,[c] Justin J. Koh,[c] Chaobin He[ac]*

a. Department of Materials Science & Engineering, National University of Singapore, 9 Engineering Drive 1, 117574, Singapore.
b. Hubei Key Laboratory of Plasma Chemistry and Advanced Materials, Hubei Engineering Technology Research Center of Optoelectronic and New Energy Materials, School of Materials Science and Engineering, Wuhan Institute of Technology, Wuhan, 430205, China.
c. Institute of Materials Research and Engineering, A*STAR (Agency for Science, Technology and Research), 138634, Singapore.

Funding: (A-Star MTC-IRG grant (No. M23M6c0107))

Keywords: biodegradable composites; thermoelectric; carbon nanotubes; polycaprolactone; energy harvesting

Abstract text.

Harvesting electricity with high-performance biodegradable thermoelectric (TE) composites is a sustainable and promising approach that addresses the environmental concerns brought from the conventional thermoelectric devices. In this work, we report a TE composite based on single-walled carbon nanotubes (SWCNT) and biodegradable polycaprolactone (PCL) with significantly improved TE performance, achieving a significant improved power factor of 439 μW m^{-1} K^{-2} at 90 wt% SWCNT loading. The good surface compatibility and interfacial interaction between PCL and SWCNT are conducive to the formation of abundant PCL-SWCNT junctions, enabling an efficient energy filtering effect that significantly enhances the Seebeck coefficient to 40.8 μV K^{-1} at SWCNT content of 90 wt%. Meanwhile, minimal charge tunneling hindrance is allowed to across thin PCL layers, thereby maintaining a high electrical conductivity of 2635 S cm^{-1}. Subsequently, a flexible TE device assembled from the SWCNT/PCL composite films exhibits a power density of 1.50 W m^{-2} at a temperature difference of 30.8 K, demonstrating great potential for high-performance and sustainable thermoelectric energy harvesting.

1. Introduction

With the explosive research on Internet of Things (IoTs) and wearable electronic devices in the past decades, the demand in power supply solutions for these devices has grown significantly.[1,2] Thermoelectric (TE) materials have emerged as promising candidates which primarily stemmed from their capability to directly convert thermal energy to electricity.[3–5] The performance of TE materials is evaluated by the dimensionless figure-of-merit ($ZT = \sigma S^2 T/\kappa$, where σ is the electrical conductivity, S is the Seebeck coefficient, T is the absolute temperature, and κ is the thermal conductivity, respectively) and power factor ($PF = \sigma S^2$). To date, inorganic TE materials such as Bi_2Te_3[6], GeTe[7] and SnSe[8], have shown high ZT values at high temperature ranges (600 – 1000 K). Despite the superior TE properties of the inorganic TE materials, they mostly consist of scarce elements with toxicity concerns and brittleness.[9,10] In contrast, organic TE materials, particularly conducting polymers such as polyaniline (PANI),[11,12] polypyrrole (PPy)[13] and poly(3,4-ethylenedioxythiophene):polystyrene sulfonate (PEDOT:PSS),[14] have been intensively studied owing to their excellent flexibility, abundancy and non-toxicity, despite of the relatively low TE properties compared to inorganic TE materials.[15,16] Moreover, composite materials based on TE materials were also widely reported with improved TE performance over organic TE materials, especially composites that integrated with carbon nanomaterials such as highly conductive carbon nanotubes (CNTs).[17–20] In addition to conducting polymers as matrix materials, insulating polymers have also been used as matrices with carbon nanomaterials to form the flexible TE composites,[21] for instance, polyvinylidene fluoride (PVDF),[22] poly (methyl methacrylate) (PMMA)[23] and polycarbonate (PC)[24]. However, these matrix materials are usually non-degradable, and the resulting electronic waste inevitably poses new environmental pollution challenges.[25] Therefore, green TE devices based on high-performance biodegradable TE composite materials become emerging alternatives to solve the problem.

Over the past few years, efforts gradually focus on integration of eco-friendly and biodegradable matrices into carbon-based TE composites to address the environmental concerns associated with conventional polymers, including natural biopolymers such as cellulose and its derivatives,[26–30] lignin,[31,32] chitin,[33] and cotton[34,35] etc., as well as synthetic biodegradable polymers, such as polylactic acid (PLA),[36,37] polyethylene oxide (PEO)[38] and polyvinyl alcohol (PVA)[39] etc. For example, Abol-Fotough et al. reported environmental-friendly CNT-embedded bacteria nanocellulose composite paper with a highest PF over 20 μW m^{-1} K^{-2}.[29] He et al. developed a CNT/chitin nanocrystal composite ink for biodegradable TE devices which exhibit a maximum PF of 0.5 μW m^{-1} K^{-2}.[33] Recently, our team also reported

an electrospun composite TE fabric based on CNT and biodegradable PLA with high Seebeck coefficient of 62.9 μV K^{-1} and an optimal PF of 0.233 μW m^{-1} K^{-2}.[36] However, vast majority of the reported carbon-based biodegradable TE composites exhibit low electrical conductivity as the biodegradable polymers are intrinsically insulating characteristics. Moreover, the biodegradable polymer addition barely increases the Seebeck coefficient of the composites at high carbon nanomaterials loadings. Therefore, there exists large limitation in the overall reported power factors of the carbon-based biodegradable TE composites (typically < 200 μW m^{-1} K^{-2}). To address this issue, strategies have been devised to enhance the TE performance of the carbon-based biodegradable TE composites such as dispersibility improvement,[31,40] doping[32] and interface engineering[41]. However, there is still a vast room for further improvement of the TE performance of carbon-based biodegradable TE composites.

Here, we report a single-walled carbon nanotubes (SWCNT)-based composite with significantly enhanced thermoelectric performance with the incorporation of biodegradable polyester polycaprolactone (PCL). Owing to the good solubility of PCL and dispersibility of SWCNT in organic solvent 1-methyl-2-pyrrolidone (NMP) as well as the interfacial compatibility with SWCNT, strong PCL adhesion on SWCNT surface was found, leading to the formation of numerous SWCNT-PCL junctions in the composites. Efficient energy filtering effect was induced between SWCNT-PCL interfacial junctions, which resulted in the significant enhancement in Seebeck coefficient of SWCNT/PCL composites. As a result, superior TE performance is achieved with an electrical conductivity of 2635 S cm^{-1}, a Seebeck coefficient of 40.8 μV K^{-1} and a maximum PF of 439 μW m^{-1} K^{-2} at SWCNT concentration of 90 wt%, which is over 3.7 times that of neat SWCNT films. We subsequently assembled a biodegradable TE device based on SWCNT/PCL composite films and cellulose substrates, which showed a maximum power density of 1.50 W m^{-2} at ΔT = 30.8 K. The high TE performance and environmental-friendly SWCNT/PCL composites thus showed great potential to be used in sustainable TEG assembly to harvest electricity from heat, which promoted the development of green energy harvesting devices to power wearable electronics.

2. Results and discussion

2.1 Morphological and physical properties of SWCNT/PCL composites

The fabrication process of SWCNT/PCL composite films is schematically depicted in **Figure 1a**. 1-methyl-2-pyrrolidone (NMP) was chosen to first disperse the SWCNT with aid of probe ultrasonication, as our previous work showed that SWCNT can be well-dispersed in NMP with smaller threads.[42] **Figure 1c-e** illustrated the SEM morphology of the neat SWCNT and

SWCNT/PCL composite films with different SWCNT loadings. In neat SWCNT films (**Figure 1h**), small intertwined nanotube threads were observed to form conductive network. With the decrease of SWCNT concentration from 90 to 50 wt% (**Figure 1e-g**), the initial dispersed small SWCNT threads gradually formed larger diameter bundles with PCL adhesion around the surface, owing to the good surface compatibility between PCL and SWCNT indicated by the small PCL melt contact angle θ (~36.7°) on SWCNT surface (**Figure 1b**). When SWCNT loading further decreased to 30 wt% (**Figure 1d**), excessive amount of PCL was found "bridging" in between the SWCNT bundles, while the gaps among SWCNT were almost filled with PCL and the SWCNT bundles were no longer easily observable with only 10 wt% of SWCNT loading (**Figure 1c**). The statistical results of SWCNT bundle diameters with different SWCNT loadings in SWCNT/PCL composite films from SEM images were shown in **Figure S1**. The neat SWCNT film prepared from NMP exhibited the lowest SWCNT average bundle diameter (μ) of 59.5 nm. With the decrease in SWCNT loadings, the average bundle diameter increases to 63.9 nm for SWCNT 90wt%/PCL composites, 74.6 nm for SWCNT 70wt%/PCL composites, 86.6 nm for SWCNT 50wt%/PCL composites, and 127 nm for SWCNT 30wt%/PCL composites, suggesting the SWCNT bundle binding by thicker PCL wrapping layers and the increased tunnelling distance between the SWCNT bundles with the decrease of SWCNT loadings. We further investigate the interfacial behavior between PCL and SWCNT using molecular dynamics (MD) simulations, as shown in **Figure 1i**. The simulated system is designed to approximate the composition of our experimental sample with 10 wt% SWCNT, representing the typical composite structure analyzed in **Figure 1c**. Based on molecular weight matching, this corresponds approximately to one SWCNT (10 nm in length, 1 nm in diameter) and one PCL chain with a degree of polymerization of 50 within a cubic simulation box of 10 × 10 × 10 nm^3 under periodic boundary conditions. The COMPASS force field is employed for all interactions, with SWCNT carbon atoms assigned a charge of zero, and PCL atomic charges derived from RESP fitting. The system is initialized at 300 K and 1 atm in the NPT ensemble and subjected to steepest descent energy minimization until the maximum force falls below 10 kJ mol^{-1} nm^{-1}. We then run MD simulations with a 2 fs time step and record snapshots every 0.1 ns up to 0.3 ns. During the simulation, we observe that the PCL chain gradually diffuses toward the SWCNT and begins to wrap around its outer wall. By 0.3 ns, a stable interfacial configuration is formed, indicating strong van der Waals interactions at the polymer-nanotube interface. This behavior is consistent with the experimentally observed encapsulation of SWCNT bundles by PCL (**Figure 1c–g**), and implies good interfacial adhesion.

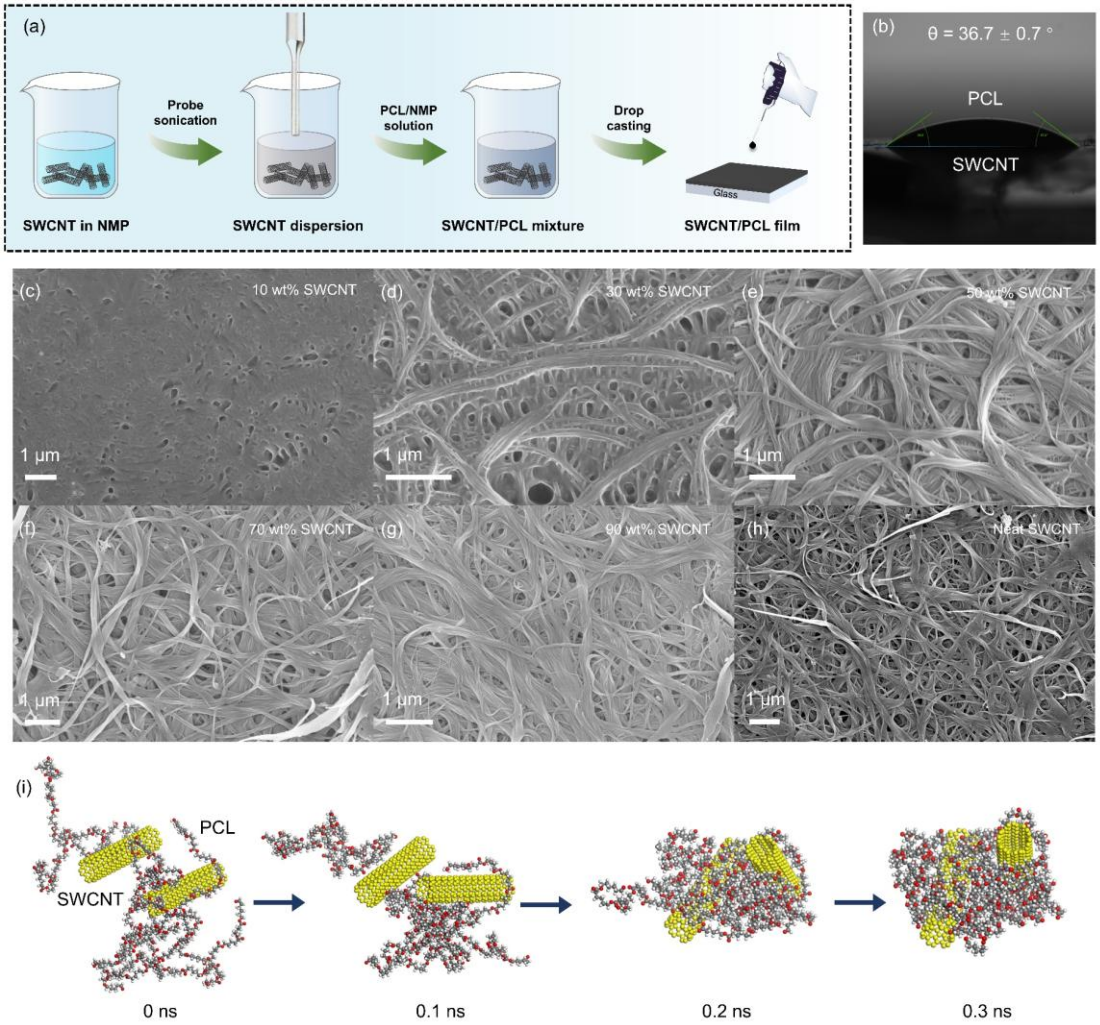

Figure 1. (a) Schematic illustration of the preparation process of the SWCNT/PCL composite film; (b) Melt contact angle θ of PCL/SWCNT interface; (c-h) SEM images of SWCNT/PCL composite films with different SWCNT loadings (10 – 90 wt%) and neat SWCNT film; (i) Molecular dynamics (MD) simulations of the interfacial behavior between PCL and SWCNT.

The interactions between SWCNT and surface-adhered PCL was further evidenced by ATR-FTIR studies. As shown in **Figure 2a** and **b**, neat PCL exhibited main characteristic peaks of stretching vibration of carbonyl group at 1720 cm^{-1}, and another two peaks at 2942 cm^{-1} and 2864 cm^{-1}, which corresponds to the asymmetric and symmetric alkyl CH_2 stretching vibrations, respectively.[43–45] It was found that the alkyl characteristic peaks gradually blue-shifted to lower wavenumbers by 5-7 cm^{-1} with increased SWCNT loadings, which may result from the intermolecular non-covalent interactions between the alkyl chain of PCL and SWCNT, such as CH-π interactions.[45–48] The C=O characteristic peak of PCL shifted to higher wavenumbers to 1731 cm^{-1} with 90 wt% of SWCNT, which is attributed to the reduced crystallinity of PCL with SWCNT incorporation.[49] **Figure 2c** and **d** show the Raman spectra of pristine SWCNT, PCL

and SWCNT/PCL composite films. The characteristic peaks of pristine SWCNT were shown in **Figure 2c**: the highly crystalline sp^2-hybridized graphitic G band (~1593 cm^{-1}) and the small D band of disordered carbon bonds or defects (~1343 cm^{-1}).[50,51] The neat PCL exhibited characteristic Raman peaks at 1440 cm^{-1} and 1720 cm^{-1}, assigned to the CH_2 bend and C=O stretch of the polyester.[52] With the addition of PCL, the G bands of SWCNT in the SWCNT/PCL composite films appeared at lower wavenumbers (~1590 cm^{-1}) as compared to the peak of pristine SWCNT. This band shift can be attributed to the noncovalent interactions between PCL and SWCNT, such as CH-π interactions and van der Waals interactions.[48,53–56] **Figure 2e** shows the XRD spectra of SWCNT, SWCNT/PCL composite films and neat PCL. As the SWCNT showed mostly amorphous structure, the XRD profiles of neat PCL and 10 wt% SWCNT/90 wt% PCL composite films were deconvoluted into three crystalline peaks at 2θ ~21.4°, 22.0° and 23.8°, which were assigned to the (110), (111), and (200) orthorhombic crystalline structures of PCL. (**Figure S2**) The full width at half maximum (FWHM) of each peak were listed in **Table S1**. Increases in broad amorphous halo and FWHM of (110) and (200) peaks for SWCNT/PCL were found with 10 wt% SWCNT loading. This indicates that the incorporation of SWCNT restricts the movement of PCL chains, leading to reduced crystallite size.[57] DSC analyses were also conducted in order to study the crystallinity and chain structures of PCL after the SWCNT integration (**Figure 2f** and **Figure S3**). The degree of crystallinity (X_c) of PCL in the SWCNT/PCL composites was calculated by:

$$\chi_c = \frac{\Delta H_f}{(1-w)\cdot \Delta H_f^0}\cdot 100\%$$

where ΔH_f is the measured heat of fusion, ΔH_f^0 is the heat of fusion of 100% crystalline PCL (135.31 J g^{-1})[58] and w is the nominal weight fraction of SWCNT in the composites. **Table S2** summarizes the peak melting temperatures (T_{mp}), enthalpy of melting (ΔH_f), and degree of crystallinity (X_c) for SWCNT/PCL composites. It was found that with the increasing amount of SWCNT integration in the PCL matrices, T_{mp} gradually decreased compared to neat PCL. Meanwhile, dramatically decreased X_c were found with higher SWCNT loading. The XRD and DSC results indicated that the PCL crystalline structures in SWCNT/PCL composites were largely affected, which is attributed to the agglomeration of excessive amount of SWCNT in PCL matrix and the presence of intermolecular interactions between SWCNT and PCL.[59,60]

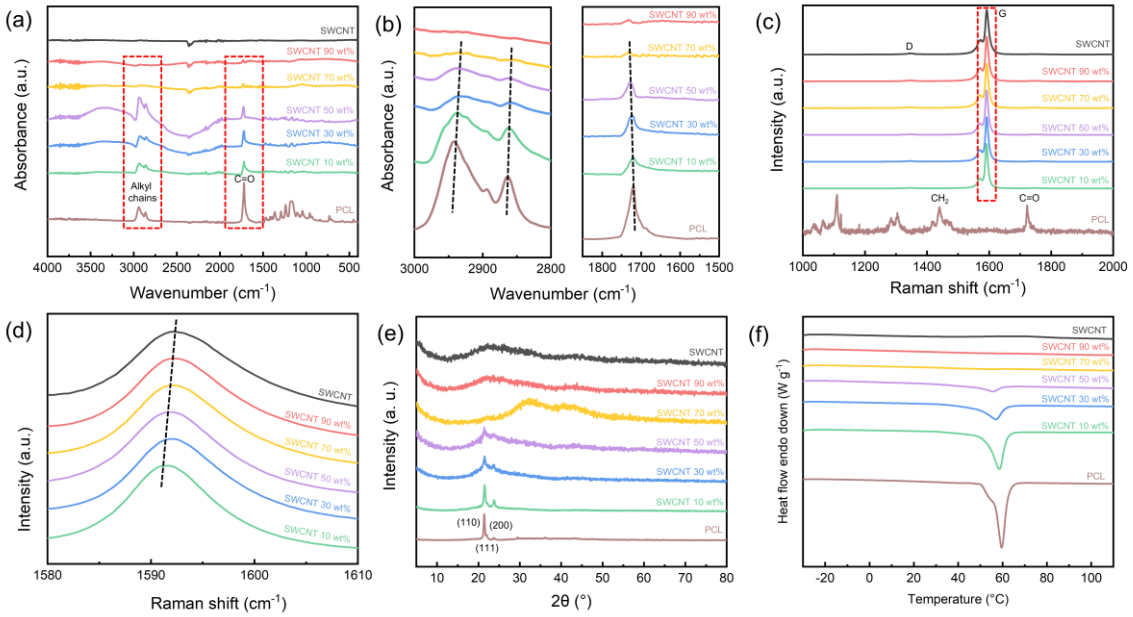

Figure 2. (a) ATR-FTIR spectra of SWCNT, PCL and SWCNT/PCL composite films, the absorption peaks around 3000 to 2800 cm^{-1} and 1850 to 1500 cm^{-1} were enlarged as (b); (c) Raman spectra of SWCNT, PCL and SWCNT/PCL composite films, the G-band around 1592 cm^{-1} were enlarged in (d); (e) XRD spectra, and (f) DSC curves of SWCNT, PCL and SWCNT/PCL composite films.

2.2 TE properties of SWCNT/PCL composites

The TE properties of the SWCNT/PCL composite films as a function of SWCNT concentration were studied, which are shown in **Figure 3a-c**. With the increasing the SWCNT concentration from 10 wt% to 90 wt%, the electrical conductivity of the SWCNT/PCL composite films increased significantly. When SWCNT concentration approached 90 wt%, the electrical conductivity of the composite film sharply increased and reached up to 2635 S cm^{-1}, which showed a slight reduction compared to that of neat SWCNT films prepared in NMP (3319 S cm^{-1}). Meanwhile, the neat SWCNT films exhibited low p-type Seebeck coefficient of only 18.7 μV K^{-1}. Interestingly, with 90 wt% of SWCNT loading, the Seebeck coefficient of the SWCNT/PCL composite films exhibited a significant enhancement to 40.8 μV K^{-1}. The Seebeck coefficient of the composite films consistently increased when SWCNT concentrations becomes lower and the highest Seebeck coefficient of 71.5 μV K^{-1} was achieved with 10 wt% SWCNT loading in the composite films. The maximum power factor of the SWCNT/PCL composite films was 439 μW m^{-1} K^{-2} at SWCNT concentration of 90 wt%, which is over 3.7 times that of neat SWCNT films prepared in NMP. Compared with the existing reports, the TE performance and power factor of our SWCNT/PCL composite are among the highest of the

biodegradable TE composites (**Figure 3f** and **Table S3**)[29,30,32–34,36,41,61–68]. The TE properties of the SWCNT 90 wt%/PCL composites with different average molecular weight of PCL were also investigated. As shown in **Figure 3d** and **e**, the highest power factor of the SWCNT 90 wt%/PCL composite films was achieved with PCL molecular weight of 10 kDa. With the increased PCL average molecular weight to 80 kDa, both lower electrical conductivity and Seebeck coefficient of the SWCNT 90 wt%/PCL composite films were observed. This phenomenon may be attributed to the decreased PCL solubility and chain mobility in NMP with higher molecular weight, which contribute to a more inhomogeneous PCL distribution among the SWCNT network,[55] which lead to the increase in charge tunneling distance between SWCNT bundles and less effective energy filtering effect in the SWCNT/PCL composites, thereby diminishing the electrical conductivity and Seebeck coefficient. In addition, the thermal conductivity of the SWCNT/PCL composites is another crucial TE property that significantly affect the TE efficiency. Neat SWCNT is often reported with large thermal conductivity from 10^0 W m^{-1} K^{-1} to such high values over 10^3 W m^{-1} K^{-1} which depends on its structure, packing density and order,[69] while the thermal conductivity of neat PCL is reported around 0.23W m^{-1} K^{-1}. [70] As for SWCNT/PCL composites, the PCL adhesion and wrapping on SWCNT surface can induce more interfacial thermal resistance for more phonon scattering to reduce the thermal conductivity compared to neat SWCNT films. Several works have reported the thermal conductivity of SWCNT-based composite films with high SWCNT loading of 70-90 wt% prepared by drop casting exhibit low out-of-plane thermal conductivity. In particular, the SWCNT-based composite films with polymer coating on its surface (such as PANI, PEDOT:PSS) exhibit thermal conductivity in a range of 0.5-0.6 W m^{-1} K^{-1}.[71–74] Therefore, we can expect thermal conductivity of the SWCNT/PCL composites to be suppressed even though the SWCNT loading is as high as 90 wt%, leading to enhanced TE efficiency.

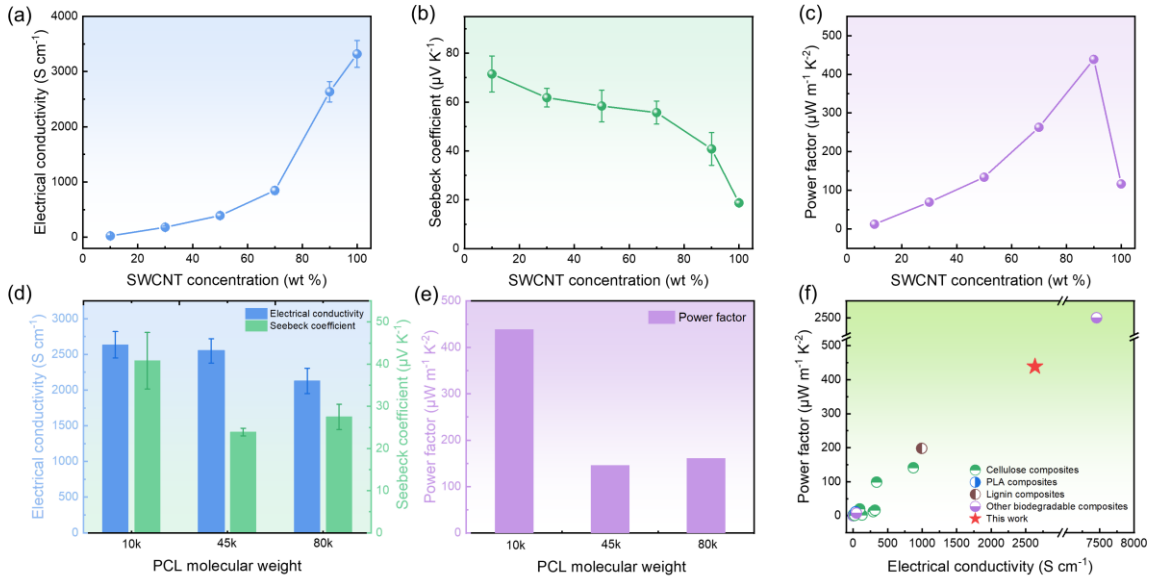

Figure 3. Thermoelectric performance of SWCNT/PCL composite films as a function of SWCNT concentration. (a) Electrical conductivity; (b) Seebeck coefficient and (c) power factors; (d) Electrical conductivity, Seebeck coefficient and (e) power factor of SWCNT 90 wt%/PCL composite films with different PCL molecular weight; (f) Comparison of power factor and electrical conductivity between this work and biodegradable composites reported in literature.

As the SWCNT concentration affected the electrical conductivity of the SWCNT/PCL composites, the charge transport mechanism of SWCNT/PCL composite films with various SWCNT loadings was investigated by measuring the temperature (T) dependence of resistances (R) of the composite films with different SWCNT concentration from 100 K to 350 K (**Figure 4a**). The $T^{-1/2}$ dependence of the normalized resistances of the neat SWCNT and SWCNT/PCL composite films were as plotted in **Figure 4b**. The R-T relationship can be well-fitted to the 1-dimensional variable range hopping (VRH) model:

$$R(T) = R_0 \exp[(\frac{T_0}{T})^{\frac{1}{2}}]$$

where $T_0 = 16/k_B N(E_F) L_{//} L_{\perp}^2$ is the characteristic temperature (k_B is the Boltzmann constant, $N(E_F)$ is the density of states at the Fermi level, $L_{//}$ and $L_{\perp}$ is the localization length in the parallel and perpendicular directions), which represents the energy barrier between localized states.[75] As shown in **Figure 4c**, the fitted T_0 values from the R-$T^{-1/2}$ curves for neat SWCNT and SWCNT/PCL composite films decreased with the increase of SWCNT concentration. The neat SWCNT films exhibited the lowest energy barrier T_0 of 0.7 K between SWCNT-SWCNT junction, while SWCNT 90 wt%/PCL composite films give slight rise to the value of T_0 to 0.9

K, where thin PCL wrapping layer poses limited hindrance to the charge carrier tunneling between the SWCNT-PCL junction, resulting in the sharp increase in the electrical conductivity when SWCNT loading approached 90 wt%. The energy barrier T_0 gradually increased to 15 K after SWCNT concentration decreased to 30 wt%, and finally increased to 292 K with 10 wt% of SWCNT integration, owing to the increased tunneling distance between the SWCNT-PCL junction with the increase PCL wrapping layer thickness. This matches the σ-T_0 relationship and is consistent to continuous declined electrical conductivity with decreased SWCNT loading (<70 wt%) in the composites.

UV–Vis-NIR absorption and UPS spectra of the SWCNT and SWCNT/PCL composite films were further collected to examine the PCL influence to the SWCNT band structures. **Figure 4d** showed the UV-Vis-NIR absorption spectra, where three main absorption peaks, namely M_{11}, S_{22}, and S_{11}, were attributed to the 1D band structure of SWCNT.[76] The band gap of pristine SWCNT was determined through a Tauc plot as illustrated in **Figure S4**. No obvious change in the absorption peaks between neat SWCNT and SWCNT 90 wt%/PCL composites were observed. Meanwhile, it is found that the two absorption peaks above 800 nm which are associated with the semiconducting optical transitions are quenched in SWCNT 10wt%/PCL composites, indicating the occupation of the conduction band by injected electrons.[76,77] The UPS investigation further confirmed the decreased work function from 4.372 eV of SWCNT to 4.315 eV (**Figure 4e** and **f**). This phenomenon can be attributed to the slight n-doping of NMP solvent on SWCNT which was trapped within the SWCNT by PCL wrapping on its surface.[78]

To elucidate the origin of the power factor enhancement in the SWCNT/PCL composites, the carrier properties of both neat SWCNT and SWCNT/PCL composite films were investigated using Hall measurements. We note that accurate determination of carrier mobility and concentration in SWCNT networks is inherently challenging due to their disordered and percolated nature.[79] Nevertheless, several studies have employed Hall measurements to characterize the carrier properties of CNT and CNT-based composite films, demonstrating the feasibility of this approach for probing carrier behavior in such systems.[80–84] As shown in **Figure 4g**, Decrease in carrier concentration with less amount of conductive SWCNT was observed, which correlated to the lower electrical conductivity and higher Seebeck coefficient. Meanwhile, carrier mobility dramatically decreased with SWCNT loading decreased below 70 wt% in the composites, on account of the thicker PCL wrapping on the SWCNT surface which largely impeded the carrier transport and hence more severe electrical conductivity loss. The inter-relationship between the Seebeck coefficient and the carrier concentration can be further expressed by Pisarenko relations which is plotted as dotted line in **Figure S5**.[85] The measured

Seebeck coefficients (S_m) of the SWCNT/PCL composite films were found much higher compared to the theoretically calculated Seebeck coefficient (S_c) based on the Pisarenko relations. The significant Seebeck enhancement in the SWCNT/PCL composites may be attributed to the formation of PCL-wrapped SWCNT structure with CH-π interactions in between, even at high SWCNT loading (>70 wt%). The energy filtering effect is thus induced at SWCNT-PCL interfaces, where energy barrier at the SWCNT/PCL interface allows high-energy carriers to cross and preferentially scatters the low-energy carriers (**Figure 4h**). Furthermore, the effect of carrier energy filtering on Seebeck enhancement can be evaluated by the ratio of S_c and S_m ($\frac{S_m-S_c}{S_c}$).[86,87] As summarized in **Table S4**, the values of $\frac{S_m-S_c}{S_c}$ first increased with decreasing SWCNT content from 90 wt% to 70 wt%, then it decreased when SWCNT loading is lower than 50 wt% in the composites. This indicates the sufficient SWCNT-PCL junctions for efficient energy filtering effect created by PCL adhesion on SWCNT surface at high SWCNT concentration (>70 wt%). However, with further decrease in SWCNT concentration to 10 wt%, the energy filtering effect would be deteriorated by scattering most of the carriers under the influence of thicker PCL coatings and stronger tunneling barriers on the SWCNT surface.

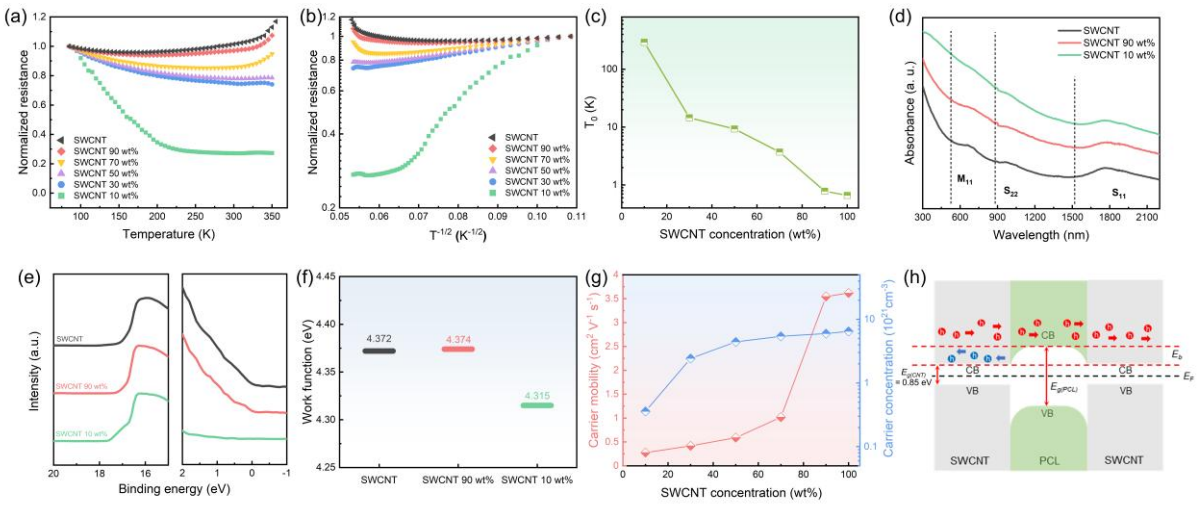

Figure 4. (a) Temperature dependence of the normalized resistance of the SWCNT/PCL composite films; (b) Analysis of R-$T^{-1/2}$ relationship of the SWCNT/PCL composite films with the VRH model; (c) Calculated energy barrier between localized states T_0 of the SWCNT/PCL composite films; (d) UV-Vis spectra, (e) UPS spectra and (f) calculated work functions of pristine SWCNT, SWCNT 10wt%/PCL and SWCNT 90 wt%/PCL composite films; (g) Carrier properties (carrier mobility and concentration) of SWCNT/PCL composite films; (h) Schematic illustration of the energy filtering effect in SWCNT/PCL composites.

2.3 TE device performance

To further verify the TE output performance of the SWCNT/PCL composite films and as a proof of concept for biodegradable green TE devices, a 5-leg TE generator was assembled with SWCNT 90 wt%/PCL composite films on cellulose film and paper substrate and connected with silver electrodes in series, which exhibited good flexibility against bending as demonstrated in **Figure 5a** and **Figure S5**. The silver electrodes were thermally cured at 50°C to ensure low contact resistance between the TE legs in the fabricated TE device ($R_{contact}$< 10Ω). Subsequently, the performance of the as-fabricated TE device on cellulose film substrates was tested with different temperature gradient (ΔT) applied to the two ends of the device. **Figure 5b** showed the open-circuit voltage of the TE device as a function of ΔT. The open-circuit voltage continuously increased with increasing ΔT and a maximum open-circuit voltage of 4.01 mV was recorded when ΔT increased to 18.8 K. The output voltage (U) and output power (P) were then measured with different external load resistances (R_{ex}) connected to the TE device under different applied ΔT = 6 K, 13.1 K and 30.8 K. As the U is defined as $U = E - IR_{int}$ (E is the open-circuit voltage of the device, R_{int} is the internal resistance of the device, and I is the output current), the U values are inversely correlated to the I at certain ΔT (**Figure 5c**). The output power P was defined as $P = EI - I^2R_{ex} = E^2R(R_{ex} + R_{int})^2$and the maximum output power P_{max} of 127.8 nW was achieved when R_{ex} of 105 Ω which equals to the R_{int} of the device at ΔT = 30.8 K (**Figure 5d**). The maximum output power density ($P_{d\ max}$) then can be calculated by $P_{d\ max} = \frac{P_{max}}{A \cdot N}$ to be 1.50 W m^{-2} at ΔT = 30.8 K, where A is the cross-sectional area of each TE leg and N is the number of TE legs (**Figure 5e**). The achieved $P_{d\ max}$ value of the TE device falls within the higher range compared to those other reported values in literature (**Table S5**).[30–34,36,41,63,64] Furthermore, as shown in **Figure 5f**, the TE device also demonstrated the capability for practical electricity harvesting from human body by generating 1.2 mV of voltage with one hand touching one end of the device. In addition, to demonstrate the mechanical stability of the TEG, we have tested the devices resistance derivation against bending deformation with various bending angles and bending cycles. As shown in **Figure 5g** and **h**, the internal device resistance maintained almost unchanged when bended by 180° and over 300 bending cycles, showing great potential in wearable applications.

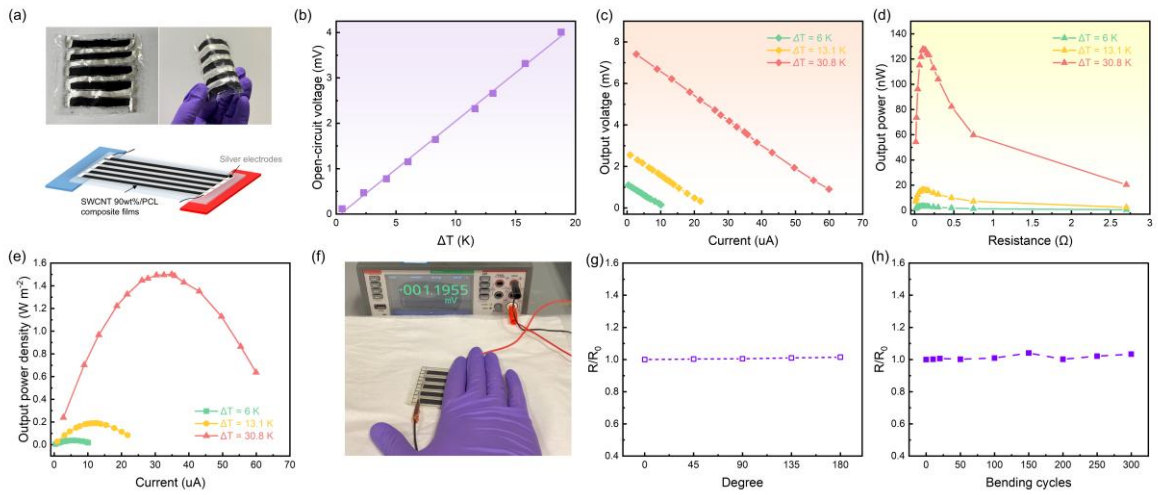

Figure 5. (a) Photo of a flexible 5-leg TEG made from 90 wt% SWCNT/10 wt% PCL composites films on cellulose film substrate; (b) Open-circuit voltage generated by the 5-leg TEG as a function of temperature; (c) The output voltage–current curve of 5-leg TEG at different temperature gradients; (d) The output power–current curve of 5-leg TEG at different temperature gradients; (e) The output power of 5-leg TEG as a function of load resistance; (f) Open-circuit voltage generated by human hands touching one end of the of 5-leg TEG; The resistance variation of the 5-leg TEG under different (g) bending degrees and (h) bending cycles.

3. Conclusion

In summary, we developed a high-performance and environmental-friendly thermoelectric (TE) composite based on single-walled carbon nanotubes (SWCNTs) and biodegradable polycaprolactone (PCL). Investigation confirmed that the good surface compatibility and the CH-π interactions between PCL and SWCNT were conducive to the formation of PCL-wrapped SWCNT structure. Hence, the significantly enhanced Seebeck coefficient to 40.8 μV K^{-1} with 90 wt% of SWCNT concentration was attributed to the sufficient SWCNT-PCL junctions created within the composites for effective energy filtering at the interface at low PCL loading. Meanwhile, the composites sustain a high electrical conductivity of 2635 S cm^{-1} with limited charge tunneling hindrance between the PCL-SWCNT interface. As a result, an outstanding power factor of 439 μW m^{-1} K^{-2} was achieved, which is over 3.7 times that of neat SWCNT films. Furthermore, a flexible biodegradable TE device assembled from SWCNT/PCL films and cellulose substrates delivered a maximum output power P_{max} of 127.8 nW and power density of 1.50 W m^{-2} under a temperature gradient of 30.8 K. This work provides a promising pathway toward development of sustainable, high-performance thermoelectric composites for future green electronics applications.

4. Experimental section

4.1 Materials

Single-walled carbon nanotubes (SWCNT) (TNSAR type, purity > 95%, < 2 nm diameter, 5-30 μm length) was purchased from Chengdu Zhongke Timesnano Co. Ltd. Polycaprolactone (average M_n~10 kDa, 45 kDa and 80 kDa) was purchased from Sigma Aldrich. 1-Methyl-2-pyrrolidone (NMP) (purity > 99%) was obtained from TCI chemicals. All other chemicals used was purchased from Sigma Aldrich.

4.2 Preparation of SWCNT/PCL composite films

SWCNT powder was added into NMP at a concentration of 2 mg ml^{-1} and probe sonicated for 15 min with sonic dismembrator (FB-120) to obtain uniform SWCNT dispersion. PCL were mixed with NMP solvent at a concentration of 0.1 g ml^{-1} and heated at 50 °C on a hotplate until all PCL flakes/pellets were fully dissolved. Then the PCL/NMP solution was added into SWCNT/NMP dispersion with designed SWCNT content to PCL (10 wt%-90 wt%) and the mixtures were stirred at 50 °C for 15 min. Afterwards, the SWCNT/PCL mixture was drop-casted on glass substrates (pre-cleaned with detergent, deionized water and ethanol) and dried on a hotplate at 50 °C for 1 day to obtain SWCNT/PCL composite films. The resultant SWCNT/PCL composite films were denoted as x wt% SWCNT, where x indicates the SWCNT concentration in the composites.

4.3 Fabrication of TE generators (TEG)

The TEG was fabricated by drop-casting SWCNT/PCL composite mixture onto cellulose film substrates [88] (or paper substrates) and dried at 50 °C to form five SWCNT/PCL composite TE legs. Each TE legs are with dimension of 5×50 mm^2 with average thickness measured around 3.4 μm and 5 mm distance apart. All five TE legs were connected in-series head to tail with silver paste.

4.4 Characterizations

The morphology of the composite films was observed by scanning electron microscope (SEM, Zeiss Sigma 300). The melt contact angle was measured with drop shape analyzer (KRUSS, DSA30). The attenuated total reflectance-Fourier transform infrared (ATR-FTIR) spectroscopy was performed on an FTIR spectrometer (Agilent Cary 660, Pike GladiATR accessory). The Raman spectroscopy was conducted using a Raman spectrometer (Horiba LabRAM HR Evolution, 514 nm Argon laser). X-ray diffraction (XRD) characterizations were conducted on an X-ray diffractometer (Bruker, D8-Advance). Differential scanning calorimetry (DSC, PerkinElmer DSC 4000) was conducted at a heating rate of 10 °C min^{-1} to from -30 to

110 °C. Electrical conductivity was measured with a Keithley 2000 bench digital multimeter using four-point probe method following Van der Pauw geometry with squared composite film samples (1.25×1.25 cm^2). The Seebeck coefficient was measured with a homemade Seebeck measuring setup, where temperature difference (ΔT) was detected by two T-type thermocouples and TE voltage (ΔV) was measured with a Keithley 2000 multimeter. The Seebeck coefficients were identified by plotting and linear fitting ΔV/ΔT plots (minimum 5 data points, $R^2 > 0.99$). The thickness of the film was determined by stylus profiler (Alpha-Step D-500). Hall measurement was conducted following Van der Pauw method with a HL5500PC Hall measurement system. Ultraviolet–visible spectroscopy (UV-Vis) of the composite films was measured on an UV-Vis spectrophotometer (Shimadzu UV-3600iPlus). Ultraviolet photoelectron spectroscopy (UPS) was performed on an X-ray photoelectron spectroscopy instrument (Thermo Scientific ESCALAB Xi^+) with negative bias (5 V) applied to sample surface. and was calibrated with pure gold foil as reference. The output voltage and power of TEG were measured by digital multimeter (Keithley DMM6500).

4.5 Simulation

Molecular dynamics simulations were performed to construct an initial model consisting of a single-walled carbon nanotube (SWCNT, 10 nanometers in length and 1 nanometer in diameter) and poly(ε-caprolactone) (PCL, with a degree of polymerization of 50). The Condensed-Phase Optimized Molecular Potentials for Atomistic Simulation Studies (COMPASS) force field was used for parameterization, with single-walled carbon nanotube carbon atoms assigned a charge of 0 and poly(ε-caprolactone) atomic charges derived from Restrained Electrostatic Potential (RESP) fitting. The system was solvated in a 10×10×10 cubic nanometer periodic boundary box, initialized at 300 Kelvin and 1 atmosphere under isothermal-isobaric (NPT) ensemble conditions. Energy minimization was performed using the steepest descent method until the maximum force fell below 10 kilojoules per mole per nanometer. Simulations were run with a 2-femtosecond time step over 0 to 0.3 nanoseconds, with configurations saved every 0.1 nanosecond.

Acknowledgements

The authors acknowledge the financial support from the A-Star MTC-IRG grant (No. M23M6c0107).

Data Availability Statement

((include as appropriate, including link to repository))

Received: ((will be filled in by the editorial staff))
Revised: ((will be filled in by the editorial staff))
Published online: ((will be filled in by the editorial staff))

References

[1] M. Gao, P. Wang, L. Jiang, B. Wang, Y. Yao, S. Liu, D. Chu, W. Cheng, Y. Lu, *Energy Environ. Sci.* **2021**, *14*, 2114.

[2] R. Liu, Z. L. Wang, K. Fukuda, T. Someya, *Nat. Rev. Mater.* **2022**, *7*, 870.

[3] T. Cao, X.-L. Shi, Z.-G. Chen, *Prog. Mater. Sci.* **2023**, *131*, 101003.

[4] S. Yang, P. Qiu, L. Chen, X. Shi, *Small Sci.* **2021**, *1*, 2100005.

[5] X.-L. Shi, J. Zou, Z.-G. Chen, *Chem. Rev.* **2020**, *120*, 7399.

[6] T. Cao, X.-L. Shi, M. Li, B. Hu, W. Chen, W.-D. Liu, W. Lyu, J. MacLeod, Z.-G. Chen, *eScience* **2023**, *3*, 100122.

[7] M. Li, X. Shi, Z. Chen, *Adv. Funct. Mater.* **2024**, *34*, 2403498.

[8] S. Bai, X. Zhang, L.-D. Zhao, *Acc. Chem. Res.* **2023**, *56*, 3065.

[9] O. Caballero-Calero, J. R. Ares, M. Martín-González, *Adv. Sustain. Syst.* **2021**, *5*, 2100095.

[10] X. Bao, S. Hou, Z. Wu, X. Wang, L. Yin, Y. Liu, H. He, S. Duan, B. Wang, J. Mao, F. Cao, Q. Zhang, *J. Mater. Sci. Technol.* **2023**, *148*, 64.

[11] S. Liu, H. Li, P. Li, Y. Liu, C. He, *CCS Chem.* **2021**, *3*, 2547.

[12] C. Zhang, H. Li, Y. Liu, P. Li, S. Liu, C. He, *Materials* **2022**, *15*, 8644.

[13] S. Xu, X.-L. Shi, M. Dargusch, C. Di, J. Zou, Z.-G. Chen, *Prog. Mater. Sci.* **2021**, *121*, 100840.

[14] H. Zhou, M. H. Chua, Q. Zhu, J. Xu, *Compos. Commun.* **2021**, *27*, 100877.

[15] Y. Zhang, W. Wang, F. Zhang, K. Dai, C. Li, Y. Fan, G. Chen, Q. Zheng, *Small* **2022**, *18*, 2104922.

[16] L. Deng, Y. Liu, Y. Zhang, S. Wang, P. Gao, *Adv. Funct. Mater.* **2023**, *33*, 2210770.

[17] Y. Bao, Y. Sun, F. Jiao, W. Hu, *Adv. Electron. Mater.* **2023**, *9*, 2201310.

[18] Y. Zhang, Q. Zhang, G. Chen, *Carbon Energy* **2020**, *2*, 408.

[19] J. L. Blackburn, A. J. Ferguson, C. Cho, J. C. Grunlan, *Adv. Mater.* **2018**, *30*, 1704386.

[20] S. Zhou, X. Shi, L. Li, Q. Liu, B. Hu, W. Chen, C. Zhang, Q. Liu, Z. Chen, *Adv. Mater.*

2025, *37*, 2500947.

[21] S. Han, S. Chen, F. Jiao, *Compos. Commun.* **2021**, *28*, 100914.

[22] T. Rodrigues-Marinho, V. Correia, C.-R. Tubio, A. Ares-Pernas, M.-J. Abad, S. Lanceros-Méndez, P. Costa, *Chem. Eng. J.* **2023**, *473*, 145297.

[23] S. Kim, Y. Song, S. H. Ryu, T.-Y. Hwang, Y. Lee, J.-H. Lim, J.-Y. Lee, K.-H. Lee, Y.-H. Choa, *Synth. Met.* **2019**, *254*, 56.

[24] Y. Zhang, L. Deng, H. Lv, G. Chen, *Npj Flex. Electron.* **2020**, *4*, 26.

[25] A. Bahrami, G. Schierning, K. Nielsch, *Adv. Energy Mater.* **2020**, *10*, 1904159.

[26] H. Cheng, Z. Wang, Z. Guo, J. Lou, W. Han, J. Rao, F. Peng, *Int. J. Biol. Macromol.* **2024**, *275*, 132908.

[27] L. Chen, J. Lou, Y. Zong, Z. Liu, Y. Jiang, W. Han, *Cellulose* **2023**, *30*, 3141.

[28] D. Palaporn, W. Mongkolthanaruk, K. Faungnawakij, K. Kurosaki, S. Pinitsoontorn, *ACS Appl. Energy Mater.* **2022**, *5*, 3489.

[29] D. Abol-Fotouh, B. Dörling, O. Zapata-Arteaga, X. Rodríguez-Martínez, A. Gómez, J. S. Reparaz, A. Laromaine, A. Roig, M. Campoy-Quiles, *Energy Environ. Sci.* **2019**, *12*, 716.

[30] J.-H. Mo, J.-Y. Kim, Y. H. Kang, S. Y. Cho, K.-S. Jang, *ACS Sustain. Chem. Eng.* **2018**, *6*, 15970.

[31] H. Zhang, H. Li, W. Wang, P. Li, S. Liu, M. Yang, C. He, *Carbon* **2024**, *229*, 119489.

[32] Y. Choi, N. T. Tran, D. Jang, M. Park, C.-J. Yoo, J. Y. Kim, H. Lee, H. Kim, *Green Chem.* **2024**, *26*, 330.

[33] Y. He, X. Lin, Y. Feng, B. Luo, M. Liu, *Adv. Sci.* **2022**, *9*, 2204675.

[34] P. Cataldi, M. Cassinelli, J. A. Heredia-Guerrero, S. Guzman-Puyol, S. Naderizadeh, A. Athanassiou, M. Caironi, *Adv. Funct. Mater.* **2020**, *30*, 1907301.

[35] W. Jiang, T. Li, B. Hussain, S. Zhou, Z. Wang, Y. Peng, J. Hu, K.-Q. Zhang, *Adv. Fiber Mater.* **2023**, *5*, 1725.

[36] S. Liu, M. Zhang, J. Kong, H. Li, C. He, *Compos. Sci. Technol.* **2023**, *243*, 110245.

[37] D. Wu, D. Lin, J. Zhang, W. Zhou, M. Zhang, Y. Zhang, D. Wang, B. Lin, *Macromol. Chem. Phys.* **2011**, *212*, 613.

[38] S. Wang, J. Wu, F. Yang, H. Xin, L. Wang, C. Gao, *ACS Appl. Mater. Interfaces* **2021**, *13*, 26482.

[39] A. G. El-Shamy, *Compos. Part B Eng.* **2019**, *174*, 106993.

[40] J. Jang, S. Kee, *Carbon* **2024**, *230*, 119590.

[41] Y. Wang, K. Li, J. Wang, X. Dai, X. Sun, D. Chong, J. Yan, L. Zhang, H. Wang, *J. Mater. Chem. A* **2022**, *10*, 25740.

[42] S. Liu, H. Li, J. C. C. Yeo, J. Kong, P. Anukunwithaya, C. He, *Carbon* **2023**, *203*, 111.

[43] J. Han, C. J. Branford-White, L.-M. Zhu, *Carbohydr. Polym.* **2010**, *79*, 214.

[44] T. Elzein, M. Nasser-Eddine, C. Delaite, S. Bistac, P. Dumas, *J. Colloid Interface Sci.* **2004**, *273*, 381.

[45] C. Funaki, S. Yamamoto, H. Hoshina, Y. Ozaki, H. Sato, *Polymer* **2018**, *137*, 245.

[46] Q. Zhang, M. Wang, H. Ao, H. Luo, X. Deng, Y. Wan, *Polym. Test.* **2021**, *96*, 107086.

[47] Y. E. Bulbul, N. Dilsiz, *Fibers Polym.* **2024**, *25*, 1701.

[48] T. Kar, H. F. Bettinger, S. Scheiner, A. K. Roy, *J. Phys. Chem. C* **2008**, *112*, 20070.

[49] K. Phillipson, M. J. Jenkins, J. N. Hay, *J. Therm. Anal. Calorim.* **2016**, *123*, 1491.

[50] M. S. Dresselhaus, G. Dresselhaus, R. Saito, A. Jorio, *Phys. Rep.* **2005**, *409*, 47.

[51] R. Saito, A. Jorio, A. G. Souza Filho, G. Dresselhaus, M. S. Dresselhaus, M. A. Pimenta, *Phys. Rev. Lett.* **2001**, *88*, 027401.

[52] A. P. Kotula, C. R. Snyder, K. B. Migler, *Polymer* **2017**, *117*, 1.

[53] A. Beigbeder, M. Linares, M. Devalckenaere, P. Degée, M. Claes, D. Beljonne, R. Lazzaroni, P. Dubois, *Adv. Mater.* **2008**, *20*, 1003.

[54] D. Baskaran, J. W. Mays, M. S. Bratcher, *Chem. Mater.* **2005**, *17*, 3389.

[55] C. A. C. Chazot, A. J. Hart, *Compos. Sci. Technol.* **2019**, *183*, 107795.

[56] M. Rahmat, P. Hubert, *Compos. Sci. Technol.* **2011**, *72*, 72.

[57] W. Ishwarchand, G. Sarakar, B. P. Swain, *Polym. Bull.* **2022**, *79*, 8437.

[58] S. Jiang, X. Ji, L. An, B. Jiang, *Polymer* **2001**, 3901.

[59] D. Xu, Z. Wang, *Polymer* **2008**, *49*, 330.

[60] J. Wang, Y. Kazemi, S. Wang, M. Hamidinejad, M. B. Mahmud, P. Pötschke, C. B. Park, *Compos. Part B Eng.* **2020**, *183*, 107663.

[61] M. Gnanaseelan, Y. Chen, J. Luo, B. Krause, J. Pionteck, P. Pötschke, H. Qi, *Compos. Sci. Technol.* **2018**, *163*, 133.

[62] L. Deng, Y. Zhang, S. Wei, H. Lv, G. Chen, *J. Mater. Chem. A* **2021**, *9*, 8317.

[63] H. Li, Y. Zong, Q. Ding, W. Han, X. Li, *J. Power Sources* **2021**, *500*, 229992.

[64] S. Kim, Y. Na, C. Nam, C. K. Jeong, K. T. Kim, K.-I. Park, *Nano Energy* **2022**, *103*, 107824.

[65] F. Jia, R. Wu, C. Liu, J. Lan, Y.-H. Lin, X. Yang, *ACS Sustain. Chem. Eng.* **2019**, 12591.

[66] H. Niu, Y. Liu, H. Song, Q. Meng, Y. Du, S. Z. Shen, *Synth. Met.* **2021**, *276*, 116752.

[67] J. Wang, H. Li, R. Liu, L. Li, Y.-H. Lin, C.-W. Nan, *Compos. Sci. Technol.* **2018**, *157*, 1.

[68] C. Yu, Y. S. Kim, D. Kim, J. C. Grunlan, *Nano Lett.* **2008**, *8*, 4428.

[69] B. Kumanek, D. Janas, *J. Mater. Sci.* **2019**, *54*, 7397.

[70] J. Wang, S. Mubarak, D. Dhamodharan, N. Divakaran, L. Wu, X. Zhang, *Compos. Commun.* **2020**, *19*, 142.

[71] G. P. Moriarty, S. De, P. J. King, U. Khan, M. Via, J. A. King, J. N. Coleman, J. C. Grunlan, *J. Polym. Sci. Part B Polym. Phys.* **2013**, *51*, 119.

[72] L. Wang, Q. Yao, J. Xiao, K. Zeng, S. Qu, W. Shi, Q. Wang, L. Chen, *Chem. – Asian J.* **2016**, *11*, 1804.

[73] C. Yu, K. Choi, L. Yin, J. C. Grunlan, *ACS Nano* **2011**, *5*, 7885.

[74] Q. Yao, Q. Wang, L. Wang, L. Chen, *Energy Env. Sci* **2014**, *7*, 3801.

[75] Z. Fan, P. Li, D. Du, J. Ouyang, *Adv. Energy Mater.* **2017**, *7*, 1602116.

[76] W. Zhou, Q. Fan, Q. Zhang, L. Cai, K. Li, X. Gu, F. Yang, N. Zhang, Y. Wang, H. Liu, W. Zhou, S. Xie, *Nat. Commun.* **2017**, *8*, 14886.

[77] Y. Liu, D. R. Villalva, A. Sharma, M. A. Haque, D. Baran, *ACS Appl. Mater. Interfaces* **2021**, *13*, 411.

[78] X. Nie, X. Mao, X. Li, J. Wu, Y. Liu, B. Li, L. Xiang, C. Gao, Y. Xie, L. Wang, *Chem. Eng. J.* **2021**, *421*, 129718.

[79] Y. Yomogida, K. Horiuchi, R. Okada, H. Kawai, Y. Ichinose, H. Nishidome, K. Ueji, N. Komatsu, W. Gao, J. Kono, K. Yanagi, *Sci. Rep.* **2022**, *12*, 101.

[80] Y. H. Kang, U.-H. Lee, I. H. Jung, S. C. Yoon, S. Y. Cho, *ACS Appl. Electron. Mater.* **2019**, *1*, 1282.

[81] S. H. Lee, T. W. Uhm, Y. G. You, S. W. Kim, S. H. Jhang, U. Dettlaff-Weglikowska, Y. W. Park, *Synth. Met.* **2014**, *198*, 84.

[82] K. T. Kim, S. Y. Choi, E. H. Shin, K. S. Moon, H. Y. Koo, G.-G. Lee, G. H. Ha, *Carbon* **2013**, *52*, 541.

[83] J. Wang, K. Cai, S. Shen, J. Yin, *Synth. Met.* **2014**, *195*, 132.

[84] H. Wang, S. Yi, X. Pu, C. Yu, *ACS Appl. Mater. Interfaces* **2015**, *7*, 9589.

[85] Z. Ma, C. Wang, J. Lei, D. Zhang, Y. Chen, Y. Wang, J. Wang, Z. Cheng, *Nanoscale* **2020**, *12*, 1904.

[86] S. Liu, H. Li, X. Fan, C. He, *Compos. Sci. Technol.* **2022**, *221*, 109347.

[87] G. Karalis, L. Tzounis, C. K. Mytafides, K. Tsirka, P. Formanek, M. Stylianakis, E. Kymakis, A. S. Paipetis, *Appl. Energy* **2021**, *294*, 117004.

[88] J. J. Koh, X. Q. Koh, J. Y. Chee, S. Chakraborty, S. Y. Tee, D. Zhang, S. C. Lai, J. C. C. Yeo, J. W. J. Soh, P. Li, S. C. Tan, W. Thitsartarn, C. He, *Adv. Sci.* **2024**, *11*, 2402390.